AIAA JOURNAL
Vol. 38, No. 7, July 2000

Analysis and Testing of Mach-Scaled Rotor with Trailing-Edge Flaps

Nikhil A. Koratkar* and Inderjit Chopra†
University of Maryland, College Park, Maryland 20742

Ongoing research is presented directed toward the development of a Mach-scaled rotor model with piezoelectric bender-actuated trailing-edge flaps for individual blade control of helicopter vibration. First, an analytical model is developed for the coupled actuator-flap-rotor dynamic response in hover. Then, the analysis is validated by using test data obtained by hover testing a 6-ft (1.82-m)-diam, Froude-scaled rotor with piezo-bender-actuated trailing-edge flaps. The analytic model shows good correlation with experimental flap deflections and oscillatory hub loads. For the Froude-scaled model flap deflections of ± 4 to ± 8 deg, for 1 to 5 /rev flap excitation, were achieved at 900 rpm. This flap activation resulted in a 10% variation in the steady rotor thrust level at 6 deg collective. Next, two Mach-scaled rotor blades with piezo-bender actuation were designed and fabricated. The rotor was tested in the vacuum chamber, and flap deflections of ± 8 deg were achieved in vacuum at the Mach-scaled operating speed of 2000 rpm. The analysis predicts that in hover flap deflections of ± 5 deg can be achieved at 2000 rpm. Future work will involve hover tests followed by forward flight tests in the wind tunnel to confirm these predictions and demonstrate concept feasibility.

Nomenclature

A_3	= coefficients of indicial function
b_3	= exponent of indicial function
C_a	= actuator damping matrix
C_b	= blade damping matrix
C_{coupling}	= coupling term in actuator damping matrix
C_H	= hinge moment coefficient
C_H^c	= circulatory hinge moment coefficient
C_H^i	= noncirculatory hinge moment coefficient
c	= airfoil chord
D	= distance of flap c.g. from feathering axis
d	= linkage arm length
E_a	= Young's modulus of actuator
E_b	= Young's modulus of shim
EI_{TOT}	= actuator cross-sectional stiffness
e	= flap hinge location (semichords)
F	= tip force acting on bender
F_b	= blade load matrix
F_4–F_{12}	= geometric constants for flap
H	= unsteady aerodynamic hinge moment
h	= total flap hinge moment
h_{CF}	= centrifugal (propeller) hinge moment
h_f	= frictional hinge moment
h_I	= inertial hinge moment
I_δ	= flap mass moment of inertia about the hinge axis
K_a	= actuator stiffness matrix
K_b	= blade stiffness matrix
K_{coupling}	= coupling term in actuator stiffness matrix
$K1$, $K2$	= noncirculatory deficiency functions
L	= unsteady lift perturbation matrix caused by trailing-edge flap motion
M	= unsteady pitching moment perturbation matrix caused by trailing-edge flap motion
M_a	= actuator mass matrix
M_b	= blade mass matrix
M_{coupling}	= coupling term in actuator mass matrix
M_{flap}	= trailing-edge flap mass
m	= mass per unit length of actuator beam
N	= amplification ratio of ac bias circuit
n	= time-step index
Q_a	= actuator load matrix
q	= vector of degree of freedom for actuator beam
R	= distance of flap midpoint from axis of rotation
r_1	= internal radius of flap hinge tube
r_2	= external radius of flap hinge tube
S	= reduced time
T	= bender kinetic energy
T_{CF}	= tensile load in actuator beam caused by centrifugal loads
T_H	= time constants for non-circulatory Indicial response
u	= degrees of freedom for blade
V	= actuator strain energy
v	= incident velocity at midpoint of flap
w	= actuator bending displacement
x	= coordinate along actuator longitudinal axis
x_{cg}	= offset of flap c.g. from hinge axis
x_5, x_6	= circulatory deficiency functions
z	= coordinate along actuator bending direction
β	= Prandtl–Glauert correction factor
ΔH	= aerodynamic hinge moment perturbation caused by blade motion terms
ΔI	= inertial hinge moment perturbation caused by blade motion terms
δ	= trailng-edge flap deflection
δW	= virtual work done by tip force, F
ε_{xx}	= strain distribution for actuator
λ	= induced strain
μ	= coefficient of friction
σ_{xx}^a	= stress in PZT
σ_{xx}^b	= stress in shim
Ω	= rotor speed

Received 19 February 1999; revision received 13 September 1999; accepted for publication 24 September 1999. Copyright © 1999 by the American Institute of Aeronautics and Astronautics, Inc. All rights reserved.

*Minta Martin Fellow, Department of Aerospace Engineering, Alfred Gessow Rotorcraft Center; nikhilk@eng.umd.edu.

†Alfred Gessow Professor and Director, Department of Aerospace Engineering, Alfred Gessow Rotorcraft Center; chopra@eng.umd.edu. Fellow AIAA.

I. Introduction

HELICOPTERS suffer from high vibration and noise levels because of the unsteady aerodynamic environment in which the blades operate, as well as the coupled structural mechanical system comprised of the rotor, fuselage, transmission system, and engine. The rotor flowfield is extremely complex and can include transonic flow on the advancing blade tip, dynamic stall on the retreating side of the disk, highly yawed and reversed flows, and blade-wake interactions with tip vortices from preceding blades. These effects give rise to unsteady aerodynamic loads at harmonics of the rotational

speed. Typically for a N-bladed rotor, the dominant $N-1$, N, and $N+1$/rev blade loads are transmitted to the fuselage as a N/rev forcing.

Reduction in vibration and noise levels of the helicopter yields benefits in improved passenger comfort, reduced crew fatigue, improved community acceptance, and increased fatigue life of structural components. Currently, passive isolators and absorbers are routinely used to reduce vibration. However, these devices cause significant weight penalties and rapidly degrade in performance away from the tuned flight condition. In contrast to traditional passive systems, active control systems are designed to cancel the vibratory forces at their source, i.e., the rotor. Higher harmonic control (HHC) systems that incorporate excitation of the swashplate at N/rev frequency with servo actuators have been shown to reduce helicopter vibration substantially.[1–3] However, this type of system has a significant weight penalty and is limited to N/rev excitation frequency of the swashplate. The limitations of HHC have spurred research in the direction of individual blade control (IBC) systems, which can control the pitch of each blade independently and at any desired frequency.[4,5] In this case hydraulic actuators are mounted in conjunction with the pitch links in the rotating frame. Primary drawbacks of this system are the high actuation power required to pitch the entire blade and the requirement for a hydraulic slip ring. Therefore, there has been growing interest in the application of smart structures technology to rotor systems.[6,7] Smart materials such as piezoceramics and magnetostrictives are suitable for IBC applications because they are compact, lightweight, provide a high bandwidth, and possess high energy densities. Blade active systems (using smart materials), such as rotors with trailing-edge flaps or controllable twist rotors, offer the advantage of IBC, require lower actuation power, and eliminate the need for a hydraulic slip ring. These on-blade active systems open up a hitherto unavailable domain for vibration control, aeromechanical stability augmentation, handling qualities enhancement, stall alleviation, and acoustic suppression.

At the University of Maryland, there has been an ongoing research activity[8–11] to control vibration actively through the activation of a trailing-edge flap using a piezoelectric bender. A number of Froude-scaled rotor models were designed and tested in hover. In earlier studies[8–10] the actuation system showed severe degradation in performance as the rotation speed approached the operating speed (from ±10 deg at 0 rpm to ±1 deg at 900 rpm). The present authors[11] conducted a series of vacuum chamber tests on a Froude-scaled model to determine the causes for the dramatic degradation in actuator performance at higher rotational speeds. The reduced performance was caused by imperfect clamping of the piezo-bender. Therefore, the bender clamping mechanism was improved to prevent slippage of the actuator under high centrifugal loads. Subsequently, flap deflections of ±6 deg at 4/rev were achieved in hover at the Froude-scaled operating speed of 900 rpm. In a parallel study Spangler and Hall[12] and Prechtl and Hall[13] at the Massachusetts Institute of Technology have designed and tested a nonrotating two-dimensional wing model with a piezo-bender-actuated trailing-edge flap. A flexure mechanism was designed to provide mechanical amplification with minimal frictional losses, and the bender was tapered to improve structural efficiency. At NASA Ames Research Center Fulton and Ormiston[14] have conducted wind-tunnel tests on a Froude-scaled rotor model with piezo-bender actuation. The tests successfully demonstrated the effectiveness of on-blade elevon controls for significantly reducing or canceling individual 3, 4, and 5/rev harmonic blade vibratory flap bending moments.

Various alternatives to piezoelectric bender actuation have also emerged. Chen and Chopra[15] developed a Froude-scaled controllable twist rotor by incorporating embedded specially shaped piezoelectric elements. Wind-tunnel tests demonstrated that the concept shows promise for partial vibration reduction. Bernhard and Chopra[16] has developed a piezo-induced bending-torsion coupled composite beam for actuating a moving blade tip. Tip deflections of ±2 deg were achieved at the Froude-scaled operating speed of 900 rpm. This actuation scheme is currently being upgraded for a Mach-scale rotor. Lee and Chopra[17] has developed an actuation mechanism for driving a full-scale trailing-edge flap using a piezo-stack device in conjunction with a double-lever amplification arrangement.

A review of the state of the art shows that Froude-scaled models have been extensively used by researchers to investigate the feasibility of smart actuation systems. Froude-scaled models are easier to design and fabricate than Mach-scaled models. However, it is well established that for vibration and acoustic studies Mach-scaled rotor models are more appropriate to simulate full-scale flight conditions. Thus, it becomes appropriate to carry out the feasibility study of a smart rotor at Mach scale. Also, available analytic studies of trailing-edge flaps[18,19] neglect the actuator dynamics and hence prescribe the trailing-edge flap motion. For a smart rotor system the actuator is coupled to the rotor response via aerodynamic and inertial coupling terms. Hence, it becomes necessary to integrate the actuator model into a comprehensive rotor analysis. This paper will address both issues: testing of a Mach-scaled model and formulation of a coupled analysis. An analytic model is developed for the coupled actuator-flap-rotor system in hover. The rotor blades are modeled as elastic beams undergoing coupled flap bending and elastic torsion. The actuator is modeled as a Bernoulli–Euler beam undergoing transverse bending deformation. The equations of motion of the actuator and rotor are coupled via aerodynamic and inertial terms. These coupled sets of equations are solved using a finite element method in space and time. The analytic model developed in this paper is validated using hover test data obtained from a previous study[11] with Froude-scaled rotor blades. The analysis shows good correlation with hover test data. Next, two Mach-scaled blades with piezoelectric bender actuation are designed and fabricated. The Mach-scaled blades are tested in the vacuum chamber to study the effect of centrifugal, inertial, and frictional loads on actuator performance. A microthrust ball bearing is incorporated at the blade-flap interface to minimize frictional losses associated with the hinge amplification mechanism. Flap deflections of ±8 deg are obtained at 2000 rpm, demonstrating the effectiveness of the actuation mechanism. Further tests are being conducted on this rotor using a Bell-412 Mach-scaled hub to evaluate the actuator performance in hover.

II. Actuation Mechanism

The bender used in this study consists of PZT-5H (lead-zirconate-titanate) piezoceramic sheets[20] that are bonded to a very thin brass shim with an electrically conductive adhesive coating (Fig. 1). The bender is cantilevered and equal, but opposite fields are applied to the PZT sheets on opposite sides of the shim. Therefore, if the PZT sheets on one side of the shim are in extension, the PZT sheets on the other side of the shim will contract and vice versa. This causes a pure bending of the actuator, and the resulting tip displacement provides the actuation mechanism for the flap. The tip displacement of the bender is small (10–20 mils) and is amplified using a mechanical leverage mechanism (Fig. 2). To adapt the bender with the linkage used for connection to the flap, a rod was molded onto the bender tip using s-glass cloth. This rod fits inside a tiny machined cusp. The cusp is an integral part of the flap. As the bender moves up

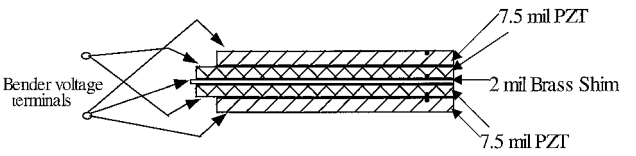

Fig. 1 Four-layered piezoelectric bender.

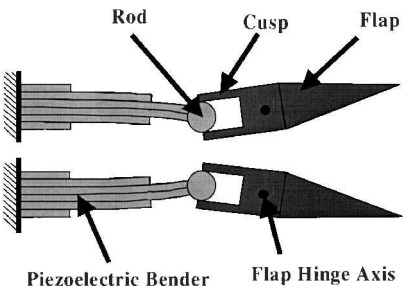

Fig. 2 Mechanical leverage mechanism.

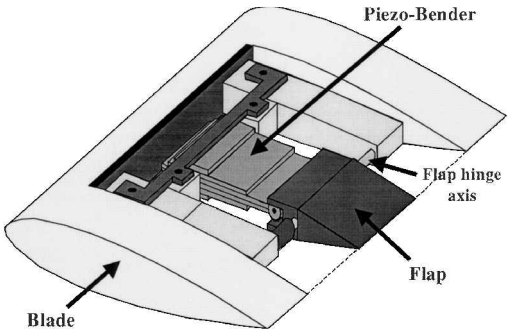

Fig. 3 Actuator-flap assembly.

and down, the molded tip moves slightly in and out of the cusp and rotates the flap. In the present design the distance between the flap hinge and bender-cusp contact point acts as the effective linkage arm length. Figure 3 shows a three-dimensional sketch of the actuator-flap assembly.

A. Advantages

This actuation scheme offers some distinct advantages and attractive features:

1) The actuator assembly is compact, allowing for multiple flaps to be located at strategic points along the blade resulting in an optimal distribution of actuation force.

2) The actuator has a very high mechanical efficiency.[13] This is because the shim is highly flexible, and hence almost the entire strain energy stored in the PZT is directly used to do useful work in deflecting the flap. Also frame compliance losses are negligible because a piezo-bender is a self-reacting actuator. A bench top test showed that an eight-layered tapered bender has a mechanical efficiency of 85%.

3) The weight penalty is moderate. For a Mach-scaled model the addition of the actuator-flap assembly and leading-edge weights for mass balancing results in a 17% increase in rotor-blade mass. For full-scale applications a 17% increase in rotor-blade mass equates to a 0.6% increase in gross takeoff weight for the Sikorsky S-76A helicopter, which is much lower than the 2% weight penalty associated with current passive vibration reduction equipment.

4) The piezoelectric bender requires low voltages (<400 V). This reduces the complexity and weight of the slip ring and associated fixtures.

5) The rod-cusp stroke amplification mechanism consisting of a single rigid lever arm is simple and can be easily implemented at full scale.

6) The linkage arm length can be adjusted to match the impedance of the actuator with the external aerodynamic spring, resulting in maximum energy efficiency.[13]

7) This actuation scheme involves a discrete actuator and does not include embedded or surface bonded components. Therefore inspection and repair can be easily carried out, leading to a robust and reliable operation.

B. Disadvantages

The actuator has two principal drawbacks:

1) The output force levels are moderate.

2) Because the actuator is mounted in the chordwise direction, mass balancing is required.

III. Analysis

The analytic model for the coupled actuator-flap-rotor system is developed in four stages. First, a time-domain, unsteady, aerodynamic model for a flapped airfoil in compressible, subsonic flow is implemented to estimate the unsteady airloads caused by flap motion. Then, a finite element model is developed to estimate the actuator-beam bending response caused by PZT excitation. The effects of centrifugal stiffening and piezo-induced strain are taken into account while formulating the actuator strain energy. The trailing-edge flap hinge moment is included in the actuator load matrix. Next, the rotor blades are modeled as elastic beams undergoing coupled flap bending and elastic torsion deformations. Finally, the rotor response equations are coupled to the actuator via aerodynamic and inertial coupling matrices. These coupled sets of equations are solved using finite element methods in space and time.

A. Aerodynamic Model

The analysis uses the time-domain, unsteady, aerodynamic model of Hariharan and Leishman.[21] This model features an indicial approach for both circulatory and noncirculatory loads caused by airfoil and flap motion. The exact indicial responses at small values of time, caused by impulsive flap motion and flap-rate perturbations, were obtained from linear, unsteady, subsonic theory in conjunction with aerodynamic reverse flow theorems. These results were then used to obtain complete asymptotic exponential approximations to the indicial responses resulting from impulsive flap deflection and flap rates. Using these indicial response functions, the unsteady airloads are calculated in the time domain as a set of recursively updated deficiency functions applied to the quasisteady aerodynamic loads. A brief description of the recursive formulation is provided next.

For arbitrary flap deflections the hinge moment coefficient is expressed as

$$C_H(S) = C_H^c(S) + C_H^i(S) \tag{1}$$

The circulatory hinge moment coefficient is

$$C_H^c(S) = -\frac{F5 - F4F10 + F12F10}{2\pi\beta}\delta_{\text{eff}}(S) \tag{2}$$

where

$$\delta_{\text{eff}}(S) = \delta^n - X_5^n \tag{3}$$

X_5 is the deficiency function associated with the circulatory hinge moment and is calculated using a one-step recursive formula

$$X_5^n = X_5^{n-1}\exp\left(-b_3\beta^2\Delta S\right) + A_3\Delta\delta \tag{4}$$

The noncirculatory hinge moment coefficient is

$$C_H^i(S) = -\frac{(1-e)^2}{2M}T_{H\delta}\left(K1_{H\delta}^n - K2_{H\delta}^n\right) \tag{5}$$

where $K1_{H\delta}$ and $K2_{H\delta}$ are noncirculatory deficiency functions expressed as follows:

$$K1_{H\delta}^n = \frac{\Delta\delta}{\Delta S} \tag{6}$$

$$K2_{H\delta}^n = K2_{H\delta}^{n-1}\exp(-\Delta S/T_{H\delta}) + \left(K1_{H\delta}^n - K1_{H\delta}^{n-1}\right) \tag{7}$$

Similarly, for an arbitrary flap-rate motion the unsteady hinge moment coefficient is expressed as

$$C_H(S) = C_H^c(S) + C_H^i(S) \tag{8}$$

The circulatory hinge moment coefficient is

$$C_H^c(S) = -\frac{F11(F12 - F4)}{4\pi\beta}\left(\frac{\dot{\delta}c}{v}\right)_{\text{eff}}(S) \tag{9}$$

where

$$(\dot{\delta}c/v)_{\text{eff}}(S) = (\dot{\delta}c/v)^n - X_6^n \tag{10}$$

X_6 is the deficiency function associated with the circulatory hinge moment and is calculated using a one-step recursive formula

$$X_6^n = X_6^{n-1}\exp\left(-b_3\beta^2\Delta S\right) + A_3\Delta(\dot{\delta}c/v) \tag{11}$$

The noncirculatory hinge moment coefficient is expressed as follows:

$$C_H^i(S) = -\frac{(1-e)^3}{6M}T_{H\delta}\left(K1_{H\dot{\delta}}^n - K2_{H\dot{\delta}}^n\right) \tag{12}$$

The noncirculatory deficiency functions are expressed as follows:

$$K1_{H\dot{\delta}}^n = \frac{\Delta(\dot{\delta}c/v)}{\Delta S} \tag{13}$$

$$K2_{H\dot{\delta}}^n = K2_{H\dot{\delta}}^{n-1}\exp(-\Delta S/T_{H\dot{\delta}}) + \left(K1_{H\dot{\delta}}^n - K1_{H\dot{\delta}}^{n-1}\right) \tag{14}$$

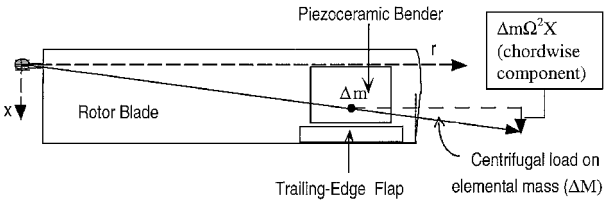

Fig. 4 Centrifugal loading on actuator.

Equations (1–14) are used to estimate the unsteady hinge moment caused by flap motion. Similar expressions are available[21] for the unsteady airfoil lift and pitching moment caused by arbitrary flap deflection and flap-rate inputs.

B. Actuator Model

The linkage arm connecting the actuator and the flap enforces a geometric compatibility between the actuator tip displacement w_{tip} and flap deflection δ. Similarly, the flap hinge moment h is directly translated into a concentrated force F acting on the bender tip. This means

$$\delta = w_{\text{tip}}/d, \qquad F = h/d \tag{15}$$

The total flap hinge moment h is composed of the aerodynamic, inertial, centrifugal (propeller), and frictional components. The kinetic energy of the bender is given by

$$T = \frac{1}{2}\int_0^L m(\dot{w})^2\,\mathrm{d}x \tag{16}$$

The centrifugal force acting on the bender in the rotating environment causes a tensile load T_{CF} in the actuator beam (Fig. 4). This tensile force results in centrifugal stiffening of the actuator beam and is expressed as

$$T_{\text{CF}}(x) = \int_0^L \Delta m\Omega^2 x \tag{17}$$

where Δm is the elemental mass of actuator beam, x is the chordwise offset of Δm from the axis of rotation, and L is the chordwise length of the bender. By adjusting the polarity of the applied electric field, the PZT sheets on the upper and lower surfaces of the brass shim are strained in opposite directions, resulting in a piezo-induced bending. The present analysis assumes that the bender behaves as a Bernoulli–Euler beam. The strain distribution caused by bending ε_{xx} is linear through the entire cross section and is given by

$$\varepsilon_{xx}(z) = z\frac{\partial^2 w}{\partial x^2} \tag{18}$$

The stress in the shim σ^b_{xx} is

$$\sigma^b_{xx}(z) = E_b\varepsilon_{xx}(z) \tag{19}$$

The stress in the PZT layers σ^a_{xx} includes the induced strain term Λ, which resembles a thermal strain

$$\sigma^a_{xx}(z) = E_a[\varepsilon_{xx}(z) - \Lambda] \tag{20}$$

The actuator strain energy V includes the induced strain term Λ as well as the centrifugal stiffening term T_{CF}:

$$\begin{aligned} V &= \frac{1}{2}\iiint_{\text{shim}} E_b(zw'')^2\,\mathrm{d}x\,\mathrm{d}y\,\mathrm{d}z \\ &\quad + \frac{1}{2}\iiint_{\text{PZT}} E_a(zw'' - \lambda)^2\,\mathrm{d}x\,\mathrm{d}y\,\mathrm{d}z + \frac{1}{2}\int_0^L T_{\text{CF}}(x)(w')^2\,\mathrm{d}x \\ &= \frac{1}{2}\int_0^L EI_{\text{TOT}}(w'')^2\,\mathrm{d}x - \frac{1}{2}\int_0^L T_{\text{CF}}(x)(w')^2\,\mathrm{d}x \\ &\quad - \int_0^L M_\lambda w''\,\mathrm{d}x + \frac{1}{2}E_a\lambda^2\int_0^L \mathrm{d}x\,\mathrm{d}y\,\mathrm{d}z \end{aligned} \tag{21}$$

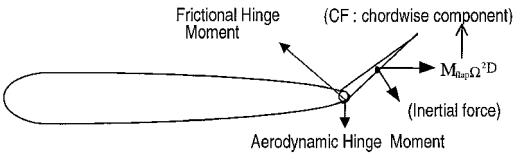

Fig. 5 Contributions to the trailing-edge flap hinge moment.

where the resulting bending stiffness, induced moment, and centrifugal loading are defined as

$$EI_{\text{TOT}} = \iint_{\text{shim}} E_b(z)^2\,\mathrm{d}y\,\mathrm{d}z + \iint_{\text{PZT}} E_a(z)^2\,\mathrm{d}y\,\mathrm{d}z$$

$$M_\Lambda = \iint_{\text{PZT}} E_a\Lambda z\,\mathrm{d}y\,\mathrm{d}z, \qquad T_{\text{CF}}(x) = \frac{m\Omega^2(L^2 - x^2)}{2}$$

The flap hinge moment h results in a tip force F on the bender [Eq. (15)]. The virtual work done by the tip force F is expressed as

$$\delta W = F\,\delta w_{\text{tip}} \tag{22}$$

The expressions for the kinetic energy, potential energy, and work done are substituted into the Lagrange equations to obtain the equations of motion for the actuator beam. Spatial discretization of the Lagrange equations results in a set of finite element equations:

$$[M_a]\ddot{q} + [K_a]q = Q_a + H(q, \dot{q}) \tag{23}$$

where Q_a is the generalized force resulting from the piezoelectric forcing M_Λ and the centrifugal, inertial, and frictional components of the flap hinge moment h. H is the generalized force related to the unsteady, aerodynamic hinge moment, which is a function of the flap deflection and velocity (Sec. III.A). Earlier experiments[11] showed that the primary source of damping in the system is the friction in the pins and linkages that rotate as the bender tip actuates the flap. To predict correctly the frequency response of the bender-flap system, this damping must be accounted for. An experiment was conducted to determine the damping ratio for the system. The actuator-flap assembly was excited at its resonant frequency, and the input voltage excitation was abruptly cut. Transient data were acquired using the real-time data acquisition and analysis package LabVIEW.[22] Using a moving-block method,[23] the damping ratio of the first mode was estimated as 0.2. Based on this value, a modal damping matrix $[C_a]$ was added:

$$[M_a]\ddot{q} + [C_a]\dot{q} + [K_a]q = Q_a + H(q, \dot{q}) \tag{24}$$

Equation (24) represents the dynamic response of the bender. The piezoelectric forcing and trailing-edge flap centrifugal, frictional, and inertial hinge moments are introduced in the load vector Q_a, while H represents the unsteady aerodynamic hinge moment caused by flap deflection and velocity. The aerodynamic hinge moment is calculated using the procedure outlined in Sec. III.A. The inertial hinge moment h_I is related to the flap mass moment of inertia about the hinge axis (Fig. 5), whereas the propeller hinge moment h_{CF} is governed by the component of the flap centrifugal loading along the chordwise direction (Fig. 5). Assuming that the trailing-edge flap deflections are small, the inertial moment h_I and propeller moment h_{CF} can be expressed as

$$h_I = I_\delta\ddot{\delta} \tag{25}$$

$$h_{\text{CF}} = M_{\text{flap}}\Omega^2 Dx_{\text{cg}}\,\delta\cdots(\sin\delta = \delta) \tag{26}$$

The frictional moment is related to the radial component of the flap centrifugal loading, which pushes the flap in the radial direction, causing the flap hinge tube to rub against the blade hinge tube surface. This creates a frictional hinge moment h_f that opposes the flap rotation:

$$h_f = \int_{r_1}^{r_2} \mu\left[\frac{M_{\text{flap}}\Omega^2 R}{\pi\left(r_2^2 - r_1^2\right)}\right]2\pi r^2\,\mathrm{d}r \tag{27}$$

The frictional hinge moment can be minimized by using a thrust bearing, which is inserted at the junction between the blade and flap hinge tubes. For a well-designed thrust bearing the coefficient of friction μ can be as low as 0.05.

C. Elastic Rotor Model

The rotor blades are modeled as elastic beams undergoing coupled flap bending and elastic torsion deformations. The formulation covers chordwise offsets of blade c.g. and aerodynamic center from the elastic axis. The equations of motion for the rotor response are derived using the Lagrange equations. Spatial discretization of the Lagrange equations results in a set of finite element equations:

$$[M_b]\ddot{u} + [C_b]\dot{u} + [K_b]u = [F_b] \tag{28}$$

where F_b is the global load vector and u is the blade nodal displacement vector. A finite element with seven degrees of freedom is used. These degrees of freedom correspond to a cubic variation in bending deflection and a quadratic variation in elastic twist. The aerodynamic loads for the rotor blades are obtained using quasi-steady aerodynamics with linear inflow assumption.

D. Actuator-Rotor Coupling

The actuator response [Eq. (24)] and rotor response [Eq. (28)] are coupled via aerodynamic and inertial terms.

1. *Aerodynamic Coupling*

The actuator tip displacement causes the trailing-edge flap to deflect [Eq. (15)]. The trailing-edge flap deflection and velocity result in an unsteady lift and pitching moment (Sec. III.A) that will augment the rotor force matrix F_b. Therefore the rotor-response equation is modified as follows:

$$[M_b]\ddot{u} + [C_b]\dot{u} + [K_b]u = [F_b] + [L(q,\dot{q})] + [M(q,\dot{q})] \tag{29}$$

The rotor elastic twist and flapwise bending velocity will result in an effective angle of attack at the trailing-edge flap. Also, the rotor twist velocity and bending acceleration will result in an angle-of-attack velocity term. Similarly, the rotor twist acceleration term will result in an angle-of-attack acceleration at the trailing-edge flap. These angle-of-attack perturbations will generate new aerodynamic hinge moments, which can be assumed to be quasi-steady.[21] Therefore Eq. (24) is modified as follows:

$$[M_a]\ddot{q} + [C_a]\dot{q} + [K_a]q = Q_a + H(q,\dot{q}) + \Delta H(u,\dot{u},\ddot{u}) \tag{30}$$

2. *Inertial Coupling*

The total mass of the actuation system and leading-edge weights for mass balancing are approximately 17% of rotor-blade mass. This change in mass distribution of the baseline blade will affect the rotor dynamics. The mass per unit length of the spatial element that contains the actuator is increased to account for the actuation system. Also the blade bending and twisting accelerations will result in inertial loads on the actuator-flap assembly (Fig. 6). Therefore, Eq. (30) is further modified as

$$[M_a]\ddot{q} + [C_a]\dot{q} + [K_a]q = Q_a + H(q,\dot{q}) + \Delta H(u,\dot{u},\ddot{u}) + \Delta I(\ddot{u}) \tag{31}$$

where ΔI is the inertial term related to the blade bending and twisting acceleration.

3. *System Response Solution*

The coupled equations of motion for the actuator [Eq. (31)] and the rotor [Eq. (29)] are used to calculate the system response:

$$\begin{pmatrix} M_a & M_{\text{coupling}} \\ 0 & M_b \end{pmatrix}\begin{Bmatrix} \ddot{q} \\ \ddot{u} \end{Bmatrix} + \begin{pmatrix} C_a & C_{\text{coupling}} \\ 0 & C_b \end{pmatrix}\begin{Bmatrix} \dot{q} \\ \dot{u} \end{Bmatrix} + \begin{pmatrix} K_a & K_{\text{coupling}} \\ 0 & K_b \end{pmatrix}\begin{Bmatrix} q \\ u \end{Bmatrix} = \begin{Bmatrix} Q_a + H(q,\dot{q}) \\ F_b + L(q,\dot{q}) + M(q,\dot{q}) \end{Bmatrix} \tag{32}$$

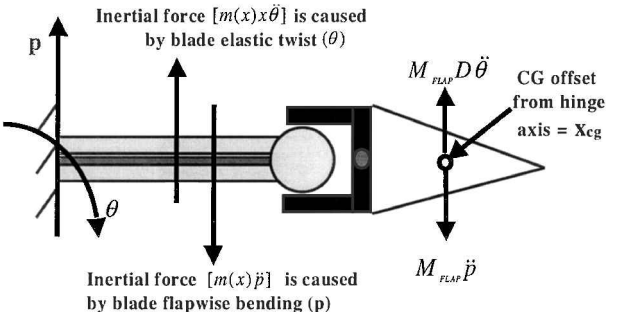

Fig. 6 Blade-motion-induced inertial loads on actuator-flap assembly.

The matrices M_{coupling}, C_{coupling}, and K_{coupling} are obtained by transfering the inertial coupling terms ΔI and the quasi-steady aerodynamic coupling terms ΔH from the right-hand side to the left-hand side of the equations. These matrices capture the feedback of blade motion on actuator response. The matrices L and M are related to the unsteady lift and pitching moment because of flap deflection and velocity (Sec. III.A). These terms represent the actuator aerodynamic coupling in the blade equations of motion.

To reduce computational time, Eq. (32) is first transformed into a set of normal mode equations. Typically, the first four blade elastic flapwise bending modes the first two blade elastic torsion modes, and the first four actuator bending modes are used for modal reduction. The periodic equations of motion are solved using the finite element-in-time method with eight equally sized time elements and fifth-order Lagrange polynomials as time basis functions. The temporal elements for a single rotor revolution are assembled so as to enforce the periodicity condition.

An iterative loop is set up for the convergence of the unsteady aerodynamic airloads associated with the H, L, and M matrices. For the first iteration the lift, pitching moment, and hinge moment deficiency functions (see Sec. III.A) are initialized to zero. Integration of the finite element-in-time matrices proceeds element by element at successively increasing values of azimuth, and the deficiency functions are updated based on the one-step recursive formula described in Sec. III.A. The final values of the lift, pitching moment, and hinge moment deficiency functions, following integration of all of the time elemental matrices, are used as the starting values in the next iteration. A simple convergence criterion is applied, based on a comparison of the initial and final values of the deficiency functions. After aerodynamic convergence is complete, the rotor hub loads are calculated using a force summation method.

IV. Typical Results and Validation

The results presented in this section are obtained for the baseline rotor tested in Ref. 11. For all of the plots presented in this section, the rotor blades are operated in a hovering condition at 900 rpm and at a collective pitch of 6 deg. The actuator is a 1-in. (2.54-cm)-long, four-layered piezo-bender excited at 95 V rms sinusoidal input. The trailing-edge flap has a 5% span and is located close to the blade tip at 95% of rotor radius. The trailing-edge flap employed in Ref. 11 is not mass balanced. The flap weighs 3.75 g, and its c.g. is located 0.2 in. (0.508 cm) behind the flap hinge axis.

Figures 7 and 8 show the influence of coupling with blade motion on actuator performance. Figure 7 indicates that the aerodynamic coupling caused by blade motion increases the amplitude of the actuator motion at 5/rev by 7.4%. Figure 8 shows that inertial coupling caused by blade motion at 3/rev does not affect the actuator response for a mass balanced flap. This is intuitively obvious because the actuator frequencies are much higher than the rotor-blade frequencies. However for the unbalanced flap used in Ref. 11, the inertial loads acting on the flap cause an 11.5% increase in the actuator deflection (Fig. 8). Figures 7 and 8 demonstrate that blade-motion coupling will affect the actuator response, and this effect should be included in smart rotor analyses. Figure 9 shows the time traces for vertical shear at the blade root for 1–5/rev trailing-edge flap excitations. For 1/rev, 2/rev, and 4/rev bender excitation, the amplitudes of oscillatory vertical shear are approximately equal [±0.35 lb (1.556 N)]. This is because these harmonics are not close to any of the rotor-blade natural frequencies. However the flap effectiveness increases

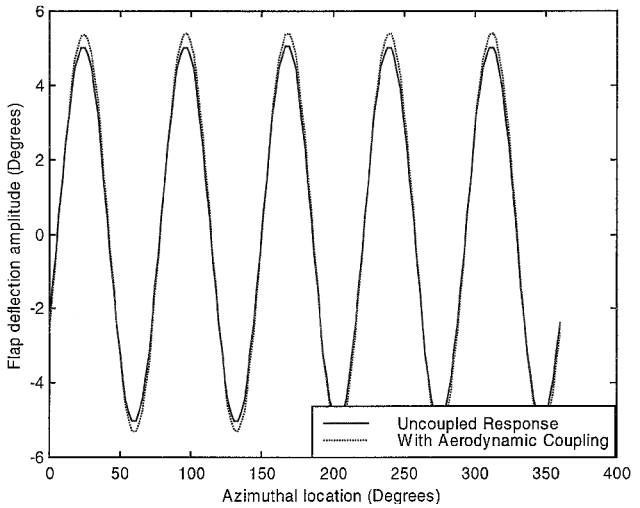

Fig. 7 Effect of aerodynamic coupling with blade motion on actuator performance at 5/rev excitation: bender excited at 95 V rms, rotor speed = 900 rpm, and collective pitch = 60 deg.

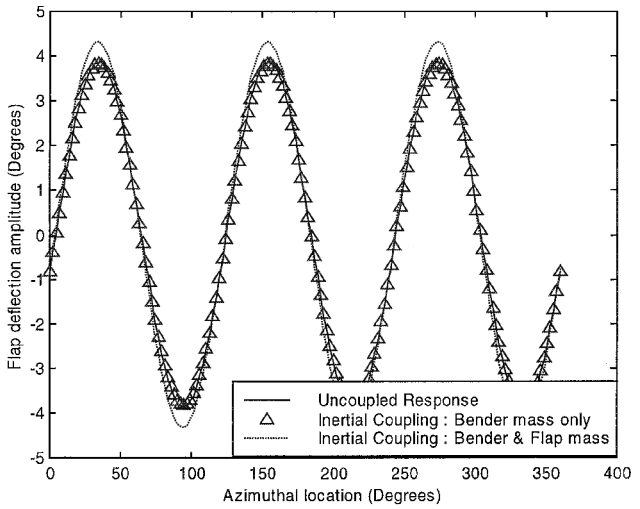

Fig. 8 Effect of inertial coupling with blade motion on actuator performance at 3/rev excitation: bender excited at 95 V rms, rotor speed = 900 rpm, and collective pitch = 6 deg.

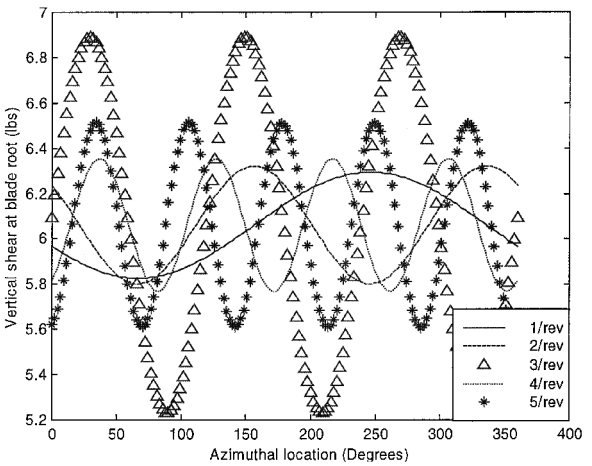

Fig. 9 Vertical shear at root of active blade caused by flap excitation: bender excited at 95 V rms, rotor speed = 900 rpm, and collective pitch = 6 deg.

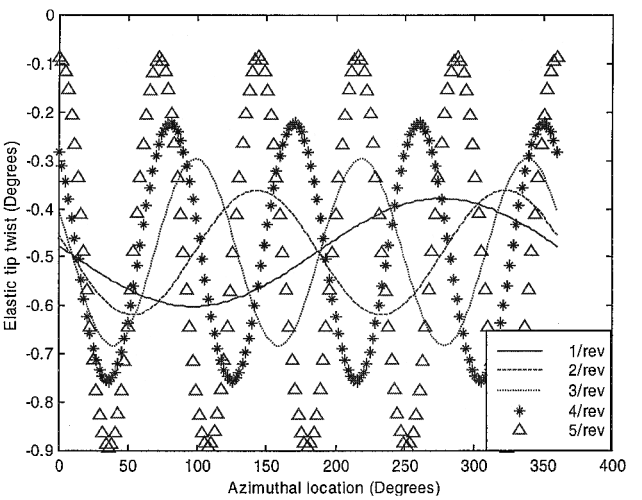

Fig. 10 Rotor blade tip twist caused by traling-edge flap excitation: bender excited at 95 V rms, rotor speed = 900 rpm, and collective pitch = 6 deg.

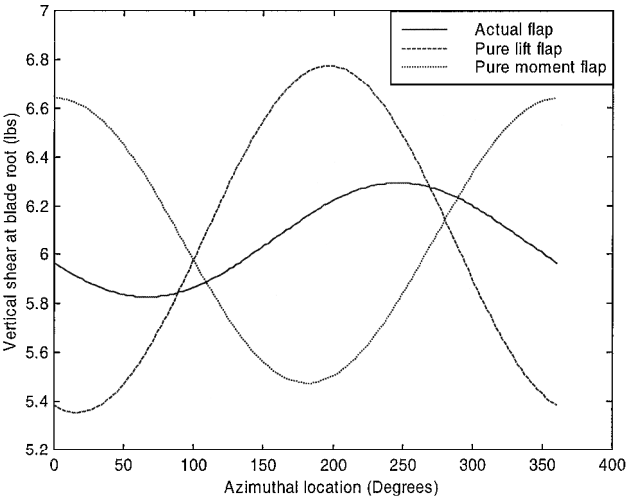

Fig. 11 Comparison of a hypothetical lift flap and moment flap with the true response for a 1/rev bender excitation: bender excited at 95 V rms, rotor speed = 900 rpm, and collective pitch = 6 deg.

at 3/rev [±0.8 lb (3.55 N)] and 5/rev [±0.5 lb (2.22 N)] because of their proximity to the rotor second flapwise bending and first torsion frequencies, respectively. Figure 10 presents the rotor-blade tip twist deformations with 1–5/rev flap excitations. The torsional frequency of the rotor[11] is 5.4/rev. Hence, the oscillatory tip twist shows an increasing trend with frequency of excitation. The oscillatory tip twist amplitude increases from ±0.11 deg (1/rev flap excitation) to ±0.45 deg (5/rev flap excitation).

Frequently, plain trailing-edge flaps that are integrated into the blade profile are characterized as lift flaps, analogous to the ailerons of a fixed-wing aircraft. For a lift flap the unsteady lift for rotor control is generated by the trailing-edge flap deflection. Moment flaps, on the other hand, generate large aerodynamic pitching moments caused by relatively large offsets between the flap and the blade elastic axis. Typically the blades are designed as torsionally soft, resulting in torsional elastic deformations. For a moment flap it is this torsional response that provides the cyclic aerodynamic lift for rotor control. The present analysis, however, indicates that even a plain trailing-edge flap that is completely integrated into the blade profile generates significant blade torsional deformation (Fig. 10). Figure 11 compares the active blade vertical shear caused by 1/rev bender excitation for the actual trailing-edge flap and a hypothetical pure-lift and pure-moment flap. For the pure-lift flap the analysis neglects the aerodynamic pitching moment generated by the flap. For the pure-moment flap the analysis neglects the unsteady lift generated by the trailing-edge flap. Figure 11 shows that the

vertical shear response generated by the moment flap and the lift flap are approximately 180 deg out of phase. Therefore for a 1/rev excitation the aerodynamic lift resulting from the blade torsional response attenuates the aerodynamic lift resulting from the trailing-edge flap deflection. Thus, the resulting response that includes both effects is much smaller than either one of these components. Figures 10 and 11 demonstrate that the trailing-edge flap cannot be characterized as a pure-lift or pure-moment device. The true response is a superposition of these two effects and will depend on the frequency of excitation and trailing-edge flap spanwise location.

A. Validation Study: Froude-Scaled Hover Testing

In Ref. 11 a two-bladed, 6-ft (1.82-m)-diam Froude-scaled, bearingless rotor model with piezoelectric bender actuation was tested on the hover stand (Fig. 12). The Froude-scaled model uses a single, four-layered bender to actuate a 5% span flap located near the tip, at 95% of rotor radius. The actuator cantilevered length is 1 in. (2.54 cm), and the linkage arm length is 54 mils. Figure 13 shows the Froude-scaled blades and the actuator-flap assembly. The details of actuator design and rotor-blade fabrication are available in Ref. 11.

The rotor hub used for these tests is a bearingless design based on the NASA/Boeing Integrated Technology Rotor program.[24] Blade flapping is achieved via a single flexbeam of varying (tapered) rectangular cross section. Pitch control is achieved through the rotation of a torsionally stiff torque tube (cuff), which is connected to the tip of the flexbeam. A detailed bearingless rotor analysis is beyond the scope of this paper. Therefore, a simplified approach was used to model the flexbeam and cuff. An averaged bending stifness and mass per unit length for the flexbeam was determined experimentally. Similarly, an effective torsional stiffness and pitch inertia for the torque tube (cuff) were also determined experimentally. The flexbeam and cuff combination was modeled using a single spatial element. The assumption was made that the flexbeam torsional stiffness is negligible compared to the cuff. The experimentally determined averaged values were then used to develop the elemental properties for the spatial element that represented the flexbeam-cuff combination. This approach gave good correlation with rotor frequencies and appears to be adequate for capturing the blade global response characteristics.

The rotor rpm is controlled by a variable-speed, water-cooled, dc motor rated for 2.5 hp at 1500 rpm. A belt and pulley arrangement connects the motor to the rotor shaft (Fig. 13). A Hall-effect sensor was used to measure the flap deflection in the rotating environment. The oscillatory hub loads were measured using a four-component rotating frame balance. A 60-channel slip ring was used for data transfer between the rotating and the fixed frames. The test data generated from these tests are used to validate the present analysis.

1. *Trailing-Edge Flap-Deflection Measurement*

RPM sweep at 15 Hz. For this test the rotor speed was steadily increased to the Froude-scaled operating speed of 900 rpm, and the bender was excited at 95 V rms and 15 Hz (1/rev). The blade collective pitch was held constant at 0 deg. Figure 14 shows the flap deflection at different rotation speeds. Flap deflections of ±4 deg were achieved at 900 rpm. There is good correlation between the analytic predictions and the experimental data. The nearly 60% reduction in actuator performance observed in Fig. 14 is caused by the aerodynamic, centrifugal, inertial, and frictional hinge moments discussed in Sec. III.B. These loads directly oppose the piezo-induced bending of the actuator beam.

Frequency sweep at 900 rpm. To establish the influence of the frequency of activation on the bender performance, a frequency sweep was conducted at the Froude-scaled operating speed of 900 rpm. The bender was excited at 95 V rms, and the blade collective pitch was set at 0 deg. The analysis shows good correlation with test data (Fig. 15). The bender natural frequency is correctly

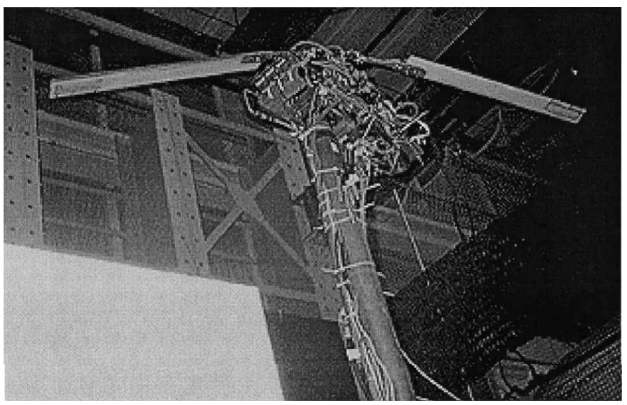

Fig. 12 Hover stand test facility.

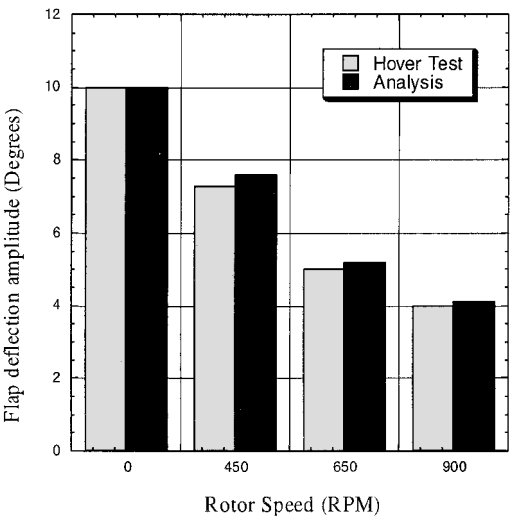

Fig. 14 RPM sweep (hover test with bender excited at 95 V rms and 15 Hz).

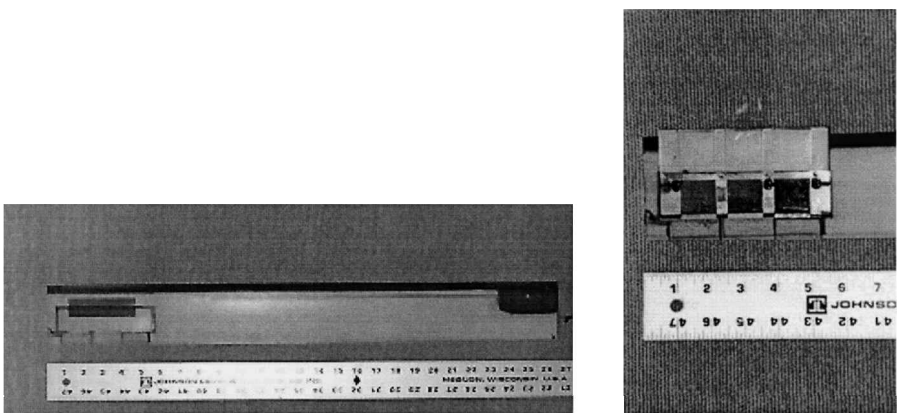

Fig. 13 Froude-scaled blade. (Four-layered piezo-bender is used to actuate a 5% span flap located at 95% of rotor radius.)

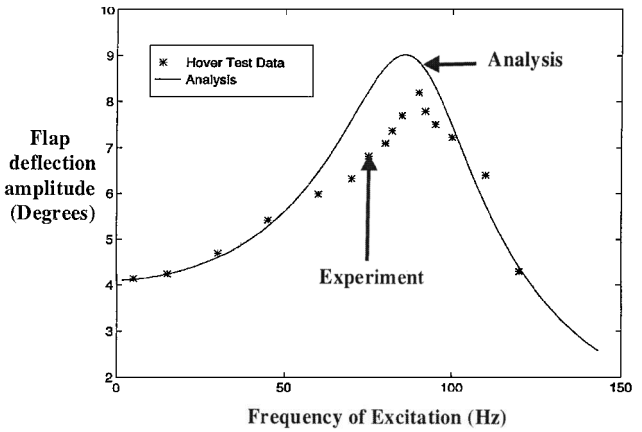

Fig. 15 Frequency sweep (hover test at 900 rpm, bender excited at 95 V rms).

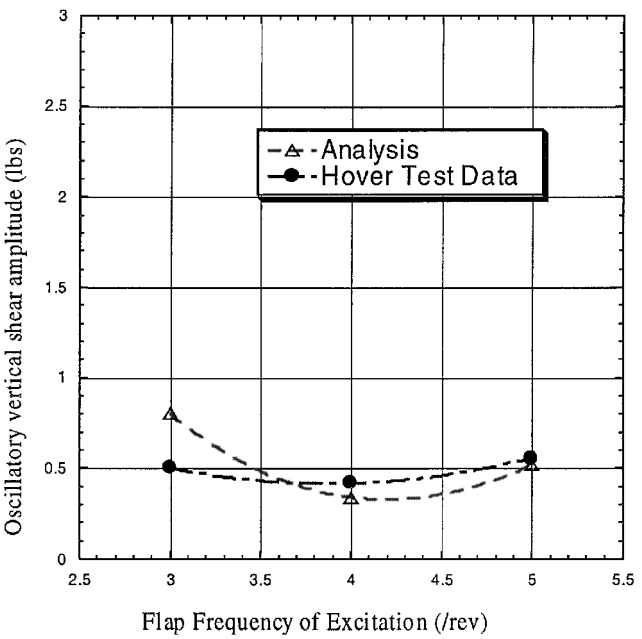

Fig. 16 Oscillatory rotor thrust caused by flap actuation at 3, 4, and 5/rev (hover test at 900 rpm and 6 deg collective, bender excited at 95 V rms).

predicted by the analysis. Flap deflections of ±4 to ±8 deg are achieved in the 1–5/rev frequency range.

2. Hub Loads Measurement

For these results the bender was excited at 95 V rms, and the rotor speed was held constant at 900 rpm. The rotor collective was set at 6 deg. The rotor thrust, flapping moment, and torque were measured using a rotating frame balance. The strain gauge signals from the rotating frame balance were amplified and filtered using a signal conditioner and analyzed using a LabVIEW[22] system. The amplitude of the oscillatory rotor thrust, flapping moment, and torque at the frequency of interest were determined by taking a fast Fourier transform of the time domain signals.

Oscillatory rotor thrust. Figure 16 compares the measured oscillatory rotor thrust with calculated values. The analysis predicts higher oscillatory rotor thrust at 3/rev and 5/rev as compared to 4/rev because of coupling with blade modes (3/rev is close to the rotor second flap-wise bending frequency and 5/rev is close to the rotor first torsion frequency). The analysis shows good correlation with test data at 4/rev and 5/rev. At 3/rev the analytic model overpredicts the oscillatory rotor thrust. The steady rotor thrust per blade at 6 deg collective is 6 lb (26.68 N). A ±0.6 lb of oscillatory thrust (Fig. 16) equates to 10% of steady thrust, thus demonstrating the feasibility of the actuation concept at Froude scale.

Table 1 Rotor-blade and trailing-edge flap parameters for Mach-scaled model

Parameter	Dimension
Rotor radius, R	3 ft (0.914 m)
Airfoil section	NACA0012
Airfoil chord	3 in. (7.62 cm)
Operating speed	2050 rpm
Tip speed	675 ft/s (205.74 m/s)
Flap span	1.75 in. (4.44 cm)
Flap chord	0.6 in. (1.52 cm)
Radial location of trailing-edge flap	$0.75R$
Blade twist	0 deg

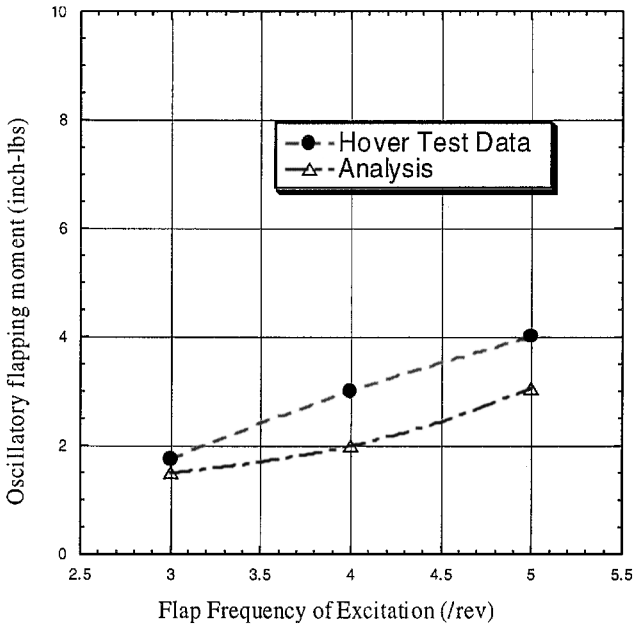

Fig. 17 Oscillatory flapping moment for 3, 4, and 5/rev flap activation (hover test at 900 rpm and 6 deg collective, bender excited at 95 V rms).

Oscillatory blade flapping moment. Figure 17 compares the measured oscillatory blade flapping moment with the predictions for 6 deg collective pitch. The analysis shows the correct trends; however, it underpredicts the oscillatory flapping moment for 4/rev and 5/rev trailing-edge flap excitation.

Oscillatory rotor torque. Figure 18 compares the measured oscillatory torque with the analysis for 6 deg collective. The analysis shows the correct trends but underpredicts the oscillatory rotor torque.

V. Proof-of-Concept Mach-Scaled Rotor Model

For vibration and acoustic studies Mach scaling is more appropriate than Froude scaling to simulate the characteristics of the full-scale system. This section presents ongoing research focused toward the development of a Mach-scaled smart rotor model. The rotor-blade and trailing-edge flap parameters are shown in Table 1.

A. Actuator Design

The operating speed for the Mach-scaled rotor is nearly two and a half times that of the Froude-scaled rotor, and this results in significantly higher aerodynamic, centrifugal, and frictional hinge moments. The four-layered bender that was incorporated into the Froude-scaled design is unable to provide sufficient actuation force to actuate the flap at Mach-scaled speeds. Therefore, an eight-layered, tapered bender (Fig. 19) was designed and fabricated in house. Increasing the number of PZT layers results in greater actuation force capability for the piezo-bender at the cost of reduced stroke. By tapering the bender, the piezo-induced bending and the

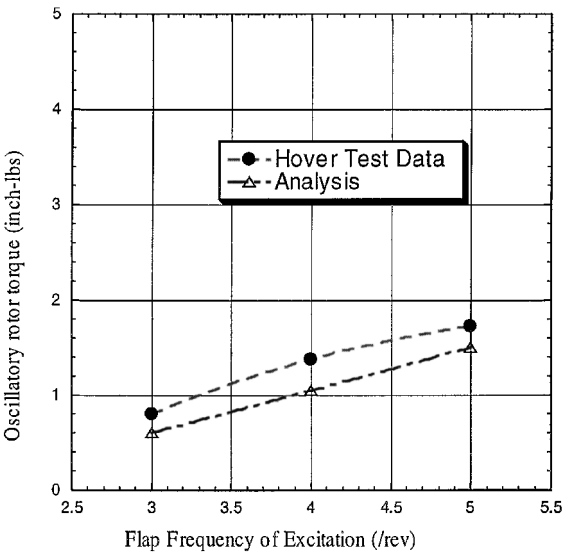

Fig. 18 Oscillatory rotor torque for 3, 4, and 5/rev flap activation (hover test at 900 rpm and 6 deg collective, bender excited at 95 V rms).

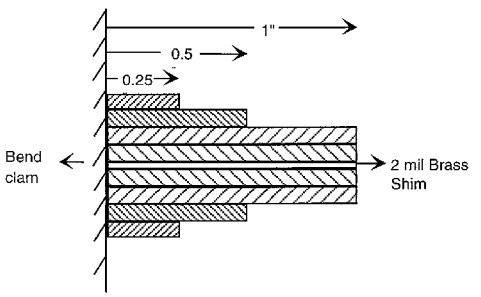

Fig. 19 Eight-layered tapered bender, used for the Mach-scaled rotor model.

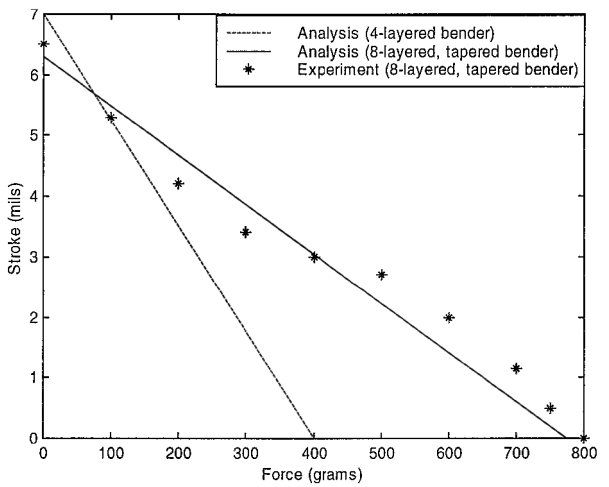

Fig. 20 Force-stroke characteristics: 1-in.-long, eight-layered, tapered actuator.

actuator stiffness are optimized, resulting in improved force-stroke characteristics. The tapering of the actuator also enables the eight-layered bender to conform to the NACA 0012 mold used to fabricate the rotor models. The eight-layered bender was tested to determine its static force and stroke characteristics (Fig. 20). The stroke (free displacement of bender tip) for the four-layered and eight-layered tapered benders are comparable; however, the superiority of the eight-layered bender over the four-layered bender lies in the actuation force output. Figure 20 shows that the block force for the eight-layered, tapered bender is about two times the corresponding value for the four-layered bender.

B. Rotor-Blade Fabrication

The aerodynamic and centrifugal loads experienced by the Mach-scaled rotor are much higher than the corresponding values for the Froude-scaled design. Consequently, most of the individual components of the rotor were redesigned to account for the higher stress levels. The primary load carrying member is a graphite-epoxy composite spar that was designed to carry a tensile force of 3800 lb (16,903 N). The graphite-epoxy spar is bolted on to an aluminum root insert, which is precision machined to match the NACA 0012 airfoil contour. Tantalum leading-edge weights are used to mass balance the blade. These leading-edge weights are embedded in specially designed rib cages (Fig. 21), which are in turn bonded to the spar using a high strength film adhesive. The anchor plate that supports the actuator-flap mechanism is also bonded to the spar using the film adhesive. This skeletal assembly is then embedded in a Rohacell IG-71 foam core, and three plies of 5-mil-thick, [0, 90] prepreg s-glass cloth are wrapped over the foam. The top and bottom surfaces of the spar get bonded to the skin as it wraps around the foam core resulting in a two-celled cross section. The aluminum root insert, with its surface area bonded to a portion of the skin, also provides a load transfer path between the skin and the composite spar. The foam core along with the skin is cured in a NACA 0012 mold. The trailing-edge flap is fabricated seperately using Rohacell foam and a single 5-mil prepreg s-glass skin. The magnet for the Hall-effect sensor is situated on the flap hinge axis and rotates with the flap via an integral arm. The flap occupies 20% of total blade chord, 5% of rotor radius, and is located at 75% radial position (Fig. 21).

C. Improved Actuator Performance Using an ac Bias Circuit

The Mach-scaled actuator consists of eight 7.5-mil thick PZT-5H sheets. For a PZT with thickness of 7.5 mil, the maximum voltage that can be applied against the direction of polarization is 140 V. Exceeding this voltage limit causes depolarization of the PZT material. However the voltage limit in the direction of polarization is much higher and is determined by dielectric breakdown and arcing of the PZT material. The PZT sheets used on the bender are driven by ac voltages, and hence the PZT sheets are excited both in and against the direction of polarization. Therefore, for a pure sinusoidal input (S in Fig. 22) the depolarization phenomenon limits the actuator performance. However the depolarization limit can be avoided by applying a larger electric field for those PZT layers that are actuated in the direction of polarization and simultaneously maintaining lower voltages (below the depoling limit) for those PZT layers that are actuated against the direction of polarization. This can be achieved using an ac bias circuit shown in Fig. 22. This circuit splits a 95-V rms waveform S into two signals S1 and S2. The signal S1 is amplified during the positive half cycle, whereas S2 is amplified during the negative half cycle. The signal S1 is applied to PZT sheets 1, 2, 3, and 4, while S2 is applied to PZT sheets 5, 6, 7, and 8 (Fig. 22). During the positive half cycle, the PZT sheets 1–4 are not in danger of being depoled, and so a large electric field can be applied (S1). Similarly, during the negative half cycle, the PZT sheets 5–8 are not in danger of being depoled, and so a large electric field can be applied (S2). The amplification factor N for the modified signals S1 and S2 can be varied, depending on the desired peak-to-peak electric field. This innovative ac bias method for piezoelectric bender actuation enables the application of large electric fields and eliminates any possibility of bender depolarization. The depoling phenomenon can also be prevented by the application of a conventional dc bias. However, this introduces a steady trailing-edge flap deflection, which will affect the steady hub loads. An advantage of the present method is that the modified waveforms (S1 and S2) do not introduce any trailing-edge flap offset angle.

D. Vacuum-Chamber Testing

The Mach-scaled rotor blades were tested in the vacuum chamber to evaluate the effectiveness of the new design. These tests reveal the effect of centrifugal, frictional, and inertial loads (except for the effect of blade flapping motion) on bender-flap performance. The vacuum chamber has a test section of 10-ft (3.04-m) diam by

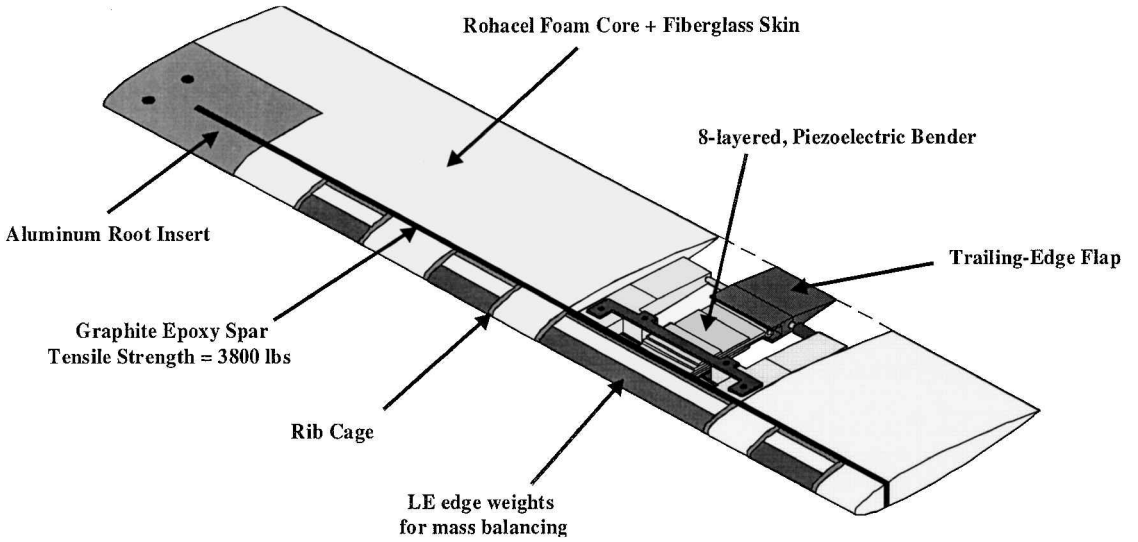

Fig. 21 Mach-scaled rotor layout.

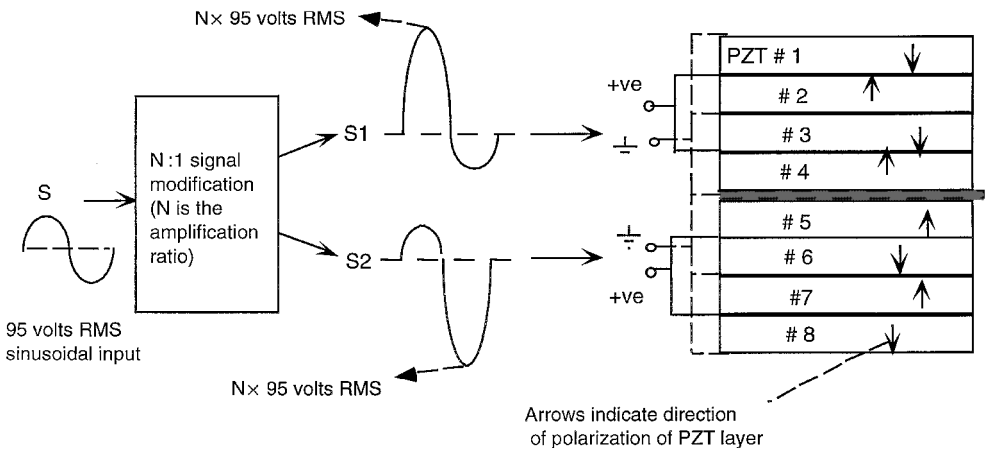

Fig. 22 AC bias circuit.

4-ft (1.21-m) height (Fig. 23) and has a rigid, nonarticulated hub that accepts signals from a 60-channel slip ring unit. The tests were conducted with the pressure inside the chamber in the 1–5 mbar range. For the present tests a linkage arm length of 80 mils was selected, and the actuator cantilevered length was 1 in. (2.54 cm).

1. Tests Without Bearing

Initial tests showed severe degradation in actuator performance at the Mach-scaled operating speed of 2000 rpm (Fig. 24). The nonrotating trailing-edge flap deflection was ±10 deg (bender excited at 95 V rms with 3:1 ac bias at 10 Hz). No significant loss in performance was observed up to 900 rpm. However, beyond that speed there was a severe reduction in performance. At 2000 rpm a maximum trailing-edge flap deflection of only ±3.2 deg was achieved. The reasons for this dramatic loss in actuator performance can be traced to the centrifugal loads associated with rotor model scale testing. For a Mach-scaled model the full-scale tip Mach number is simulated. However, the centrifugal loading is overscaled. For the present rotor model the model g loading (3500 g) caused by centrifugal action is approximately five times the full-scale g loading. This high centrifugal forcing results in large frictional losses at the blade flap interface, causing degradation in actuator performance. Still, Mach-scale testing is necessary to demonstrate that the blade control system can overcome vibratory airloads caused by transonic effects.

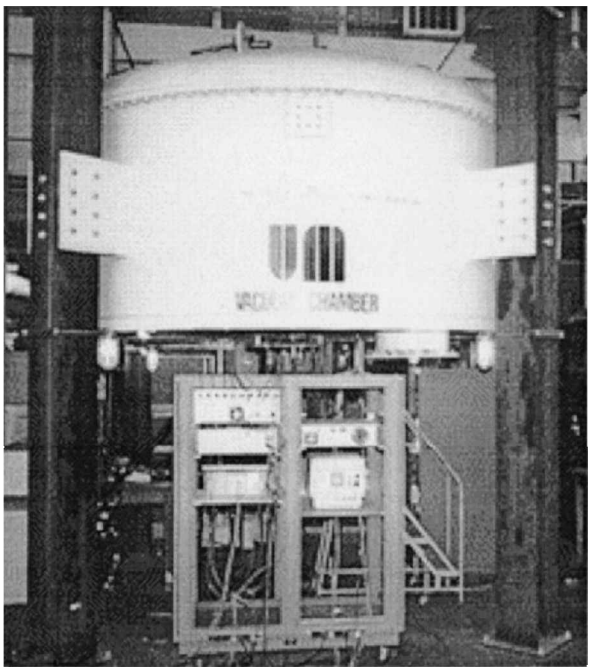

Fig. 23 Vacuum-chamber test facility.

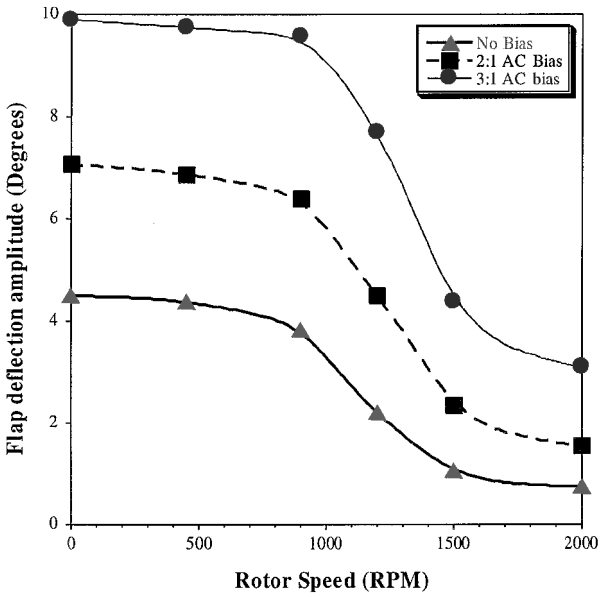

Fig. 24 Vacuum-chamber test for Mach-scaled rotor without thrust bearing (rpm sweep with a 10-Hz excitation).

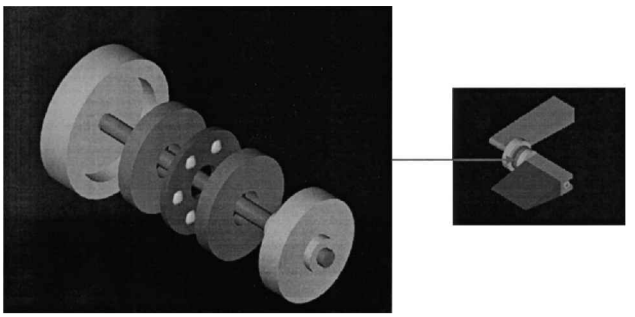

Fig. 25 Thrust-bearing assembly.

2. Installation of a Thrust Bearing

For full-scale applications a thrust bearing can be easily incorporated to minimize frictional losses. However, at model scale size limitations preclude the use of a conventional roller thrust bearing. For the present study a microthrust ball bearing (F2-6) was selected. This bearing has a bore diameter of 2 mm, outside diameter of 6 mm, static load capacity of 19.39 lb (86.25 N), and dynamic load capacity of 26.44 lb (117.61 N). Because the shaft that hinges the flap has a diameter of only 1 mm, the bearing cannot be directly mounted on the shaft. As a result, specially designed sleeves (Fig. 25) were precision machined to act as interfaces between the bearing and the shaft. For ideal operation the F2-6 bearing should provide a coefficient of friction μ of 0.05.

3. Tests with Bearing

First, an rpm sweep was performed for a 10-Hz bender excitation. The eight-layered piezo-bender was excited at 95 V rms with a 3:1 ac bias ($N = 3$). A trailing-edge flap-deflection amplitude of ± 7.7 deg was achieved at 2000 rpm (Fig. 26). With the incorporation of the thrust bearing, the actuator performance has more than doubled. The analytic model (with $\mu = 0.05$) shows good correlation with the test data. Next, a frequency sweep was performed at 2000 rpm. For a 40-Hz excitation flap-deflection amplitude of ± 8.6 deg was obtained (Fig. 27). Figures 26 and 27 clearly illustrate that, with the incorporation of a thrust bearing, the actuation mechanism is able to overcome the centrifugal, inertial, and frictional loads.

E. Predicted Response in Hover

The design goal for the Mach-scaled smart rotor is to achieve ± 4 to ± 8 deg of trailing-edge flap deflection in hover in the 1–5/rev frequency range. Because a thrust bearing is being used, a coefficient

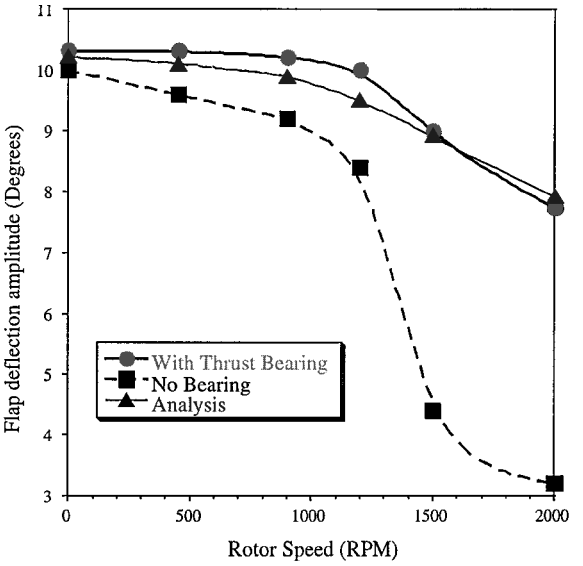

Fig. 26 Vacuum-chamber test for Mach-scaled model with thrust bearings (rpm sweep at 10 Hz, bender excited at 95 V rms with 3:1 ac bias).

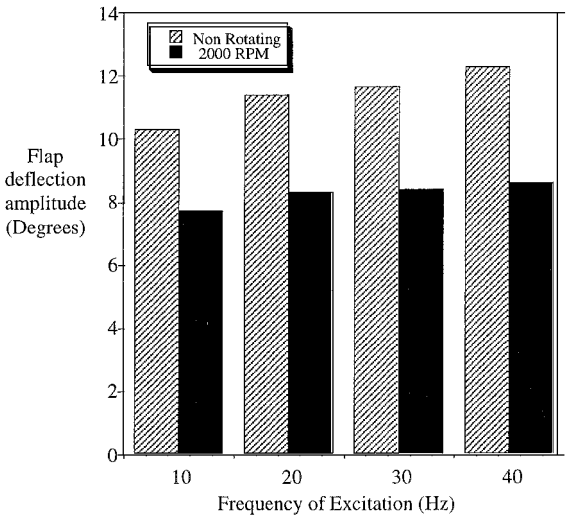

Fig. 27 Vacuum-chamber test for Mach-scaled model with thrust bearings (frequency sweep at 2000 rpm, bender excited at 95 V rms with 3:1 bias).

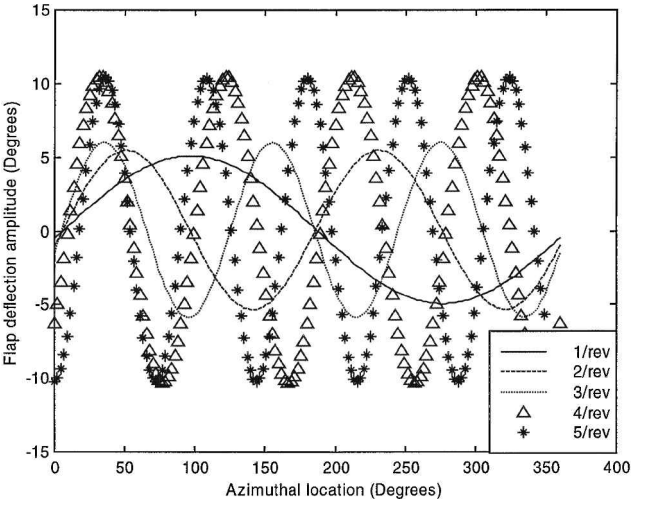

Fig. 28 Predicted response in hover for Mach-scaled model with thrust bearings (rotor speed = 2000 rpm, collective pitch = 6 deg, bender excited at 95 V rms with 3:1 ac bias).

of friction of 0.05 is selected for the analysis. The optimum linkage arm length for the Mach-scaled configuration was found to be 80 mils. The analysis indicates that the 1 in. long, eight-layered, tapered bender excited at 95 V rms (with 3:l ac bias), with a lever arm of 80 mils, can deflect the trailing-edge flap by ±5 to ±10 deg at 2000 rpm in hover (Fig. 28).

VI. Conclusion

This research project is part of the continuing development of a smart helicopter rotor system, using an active trailing-edge flap for individual blade control of vibration. The actuation mechanism for the trailing-edge flap is based on a solid-state, induced-strain, piezoelectricbender. An analytic model is developed for the coupled actuator-flap-rotor response in hover. Because the actuator model is integrated into the rotor analyses, the present formulation does not require the trailing-edge flap motion to be prescribed as an independent input. The only prescribed input parameter for the present analysis is the voltage input to the actuator at every azimuthal time step. The only constraint is that the voltage input must retain periodicity over one revolution, which is required for rotor vibration control. To validate the analytic model, Froude-scaled hover test data from Ref. 11 were used. Good correlation of predicted results with test data was obtained. Flap deflections of ±4 to ±8 deg were achieved in the 1–5/rev frequency range at the Froude-scaled operating speed of 900 rpm. The flap actuation resulted in a 10% variation in the steady rotor thrust at 6-deg collective pitch.

For the Mach-scaled rotor the piezoelectric bender force output required to overcome the trailing-edge flap hinge moments is much larger than that for a Froude-scaled model. Therefore, to achieve the desired flap authority, the following design improvements were implemented for the actuation system:

1) The four-layered actuator used in the Froude-scaled design was replaced with an eight-layered, tapered bender. This doubles the actuation force output without a significant reduction in the stroke.

2) The actuator force-stroke response is further improved by the use of a modified input signal (ac bias circuit). For a 3:1 amplification the actuator force and stroke levels are doubled.

3) Preliminary Mach-scaled tests conducted inside a vacuum chamber revealed that the major source of performance degradation at Mach-scaled g loadings is the friction at the blade-flap interface. Consequently a microthrust bearing (F2-6) was specially mounted on the flap shaft to minimize frictional losses at the blade-flap interface.

With the inclusion of the thrust bearing, flap deflections of over ±8 deg were recorded at 2000 rpm in the vacuum chamber. The analysis predicts that with the thrust bearing trailing-edge flap deflections of ±5 to ±10 deg can be achieved in the 1–5/rev frequency range, in hover at the Mach-scaled operating speed of 2000 rpm. Future work will include hover testing, followed by wind-tunnel testing. Also the actuator model developed in this paper will be integrated with a comprehensive rotor analysis such as UMARC, so that the vibration suppression capabilities of the piezoelectric bender can be analyzed in more challenging flight regimes.

Acknowledgments

This work was funded by the Army Research Office under Grant DAAH-04-96-10334 with Gary Anderson and Tom Doligalski serving as technical monitors.

References

[1]Nguyen, K., and Chopra, I., "Application of Higher Harmonic Control to Rotors Operating at High Speed and Thrust," *Journal of the American Helicopter Society*, Vol. 35, No. 3, 1990, pp. 78–89.

[2]Shaw, J., Albion, N., Hanker, E. J., and Teal, R. S., "Higher Harmonic Control: Wind Tunnel Demonstration of Fully Effective Vibratory Hub Forces Suppression," *Journal of the American Helicopter Society*, Vol. 34, No. 1, 1989, pp. 14–25.

[3]Wood, E. R., Powers, R. W., Cline, C. H., and Hammond, C. E., "On Developing and Flight Testing a Higher Harmonic Control System," *Journal of the American Helicopter Society*, Vol. 30, No. 1, 1985, pp. 3–20.

[4]Ham, N. D., "Helicopter-Individual Blade Control Research at MIT 1977–1985," *Vertica*, Vol. 11, No. 1/2, 1987, pp. 109–122.

[5]Jacklin, S. A., Blaas, A., Teves, D., and Kube, R., "Reduction in Helicopter BVI Noise, Vibration and Power Consumption Through Individual Blade Control," *Proceedings of the 51st Annual Forum of American Helicopter Society*, American Helicopter Society, Alexandria, VA, 1995.

[6]Straub, F. K., "A Feasibility Study of Using Smart Materials for Rotor Control," *Journal of Smart Materials and Structures*, Vol. 5, No. 1, 1995, pp. 68–75.

[7]Chopra, I., "Status of Application of Smart Structures Technology to Rotorcraft Systems," June 1997.

[8]Samak, D. K., and Chopra, I., "A Feasibility Study to Build a Smart Rotor: Trailing-Edge Flap Actuation," *Proceedings of the SPIE Conference on Smart Structures and Materials*, 1993.

[9]Walz, C., and Chopra, I., "Design and Testing of a Helicopter Rotor Model with Smart Trailing Edge Flaps," *Proceedings of the 35th AIAA Structures, Structural Dynamics and Materials Conference, Adaptive Structures Forum*, AIAA, Washington, DC, 1994.

[10]Ben-Zeev, O., and Chopra, I., "Development of an Improved Rotor Model with Smart Trailing Edge Flaps," *Journal of Smart Materials and Structures*, Vol. 5, No. 1, 1996, pp. 11–25.

[11]Koratkar, N. A., and Chopra, I., "Analysis and Testing of a Froude-Scaled Rotor with Piezolectric Bender Actuated Trailing-Edge Flaps," *Journal of Intelligent Material Systems and Structures*, Vol. 8, No. 7, 1997, pp. 555–570.

[12]Spangler, R. L., and Hall, S. R., "Piezoelectric Actuators for Helicopter Rotor Control," *Proceedings of the 31th AIAA/ASME/ASCE/AHS Structures, Structural Dynamics, and Materials Conference*, AIAA, Washington, DC, 1990.

[13]Prechtl, E. F., and Hall, S. R., "Development of a Piezoelectric Servoflap for Helicopter Rotor Control," *Journal of Smart Materials and Structures*, Vol. 5, No. 1, 1996, pp. 26–34.

[14]Fulton, M. V., and Ormiston, R. A., "Hover Testing of a Small-Scale Rotor with On-Blade Elevons," *Proceedings of the 53rd Forum of the American Helicopter Society*, American Helicopter Society, Alexandria, VA, 1997.

[15]Chen, P. C., and Chopra, I., "Development of a Smart Rotor Blade with Induced Strain Actuation of Blade Twist," *AIAA Journal*, Vol. 35, No. 1, 1997, pp. 6–11.

[16]Bernhard, A., and Chopra, I., "Development of a Smart Moving Blade Tip Activated by a Piezo Induced Bending-Torsion Coupled Beam," *Society of Photo-Optical Instrumentation Engineers*, Feb. 1996.

[17]Lee, T., and Chopra, I., "Development of a Smart Rotor with Piezo-Stack Actuation," *Proceedings of the 1998 SPIE'S Symposium on Smart Structures and Materials*, 1998.

[18]Milgram, J. H., and Chopra, I., "Rotors with Trailing-Edge Flaps: Analysis and Comparison with Experimental Data," *Journal of the American Helicopter Society*, Oct. 1998, pp. 319–331.

[19]Millot, T. A., and Friedman, P. P., "The Implementation of an Actively Controlled Flap to Reduce Vibrations in Helicopter Rotors," *Proceedings of the 49th Annual Forum of the American Helicopter Society*, American Helicopter Society, Alexandria, VA, 1993, pp. 1079–1092.

[20]Morgan Matroc Inc. Electro Ceramics Division, "Guide to Piezoelectric Ceramics," Manufacturer's Data Sheet, Morgan Matroc, Inc., Bedford, OH, May 1993.

[21]Hariharan, N., and Leishman, J. G., "Unsteady Aerodynamics of a Flapped Airfoil in Subsonic Flow by Indicial Concepts," *Journal of Aircraft*, Vol. 33, No. 5, 1996, pp. 855–868.

[22]National Instruments, "LabVIEW for Mac.—Data Acquisition Manual," Aug. 1993.

[23]Tasker, F. A., and Chopra, I., "Assessment of the Transient Analysis Techniques for Rotor Stability Testing," *Journal of the American Helicopter Society*, Jan. 1990, pp. 39–50.

[24]Mychalowycz, E. M., "ITR/FRR Design, Test Plan-Wind Tunnel Test," Boeing-Vertol Company Interoffice Memorandum, 3-7452-1-1216 Rev A, Nov. 13, 1984.

A. Chattopadhyay
Associate Editor